J. Cent. South Univ. (2021) 28: 3190−3206
DOI: https://doi.org/10.1007/s11771-021-4791-x

Springer

Mechanical behavior of deep sandstone under high stress-seepage coupling

ZHANG Jun-wen(张俊文)[1], SONG Zhi-xiang(宋治祥)[1]*, WANG Shan-yong(王善勇)[2]

1. School of Energy and Mining Engineering, China University of Mining and Technology (Beijing), Beijing 100083, China;
2. Priority Research Centre for Geotechnical Science & Engineering, the University of Newcastle, Callaghan, NSW 2308, Australia

© Central South University Press and Springer-Verlag GmbH Germany, part of Springer Nature 2021

Abstract: The mechanical behavior evolution characteristics of sandstone are important to the application and practice of rock engineering. Therefore, a new method and concept of deep rock mechanics testing are proposed to reveal the mechanical behavior evolution mechanism of deep roadway surrounding rock after excavation with a depth over 1000 m. High stress-seepage coupling experiments of deep sandstone under various confining pressures are conducted using GCTS. Stress−strain and permeability curves are obtained. The three-stage mechanical behavior of deep sandstone is better characterized. A platform and secondary compaction phenomena are observed. With the confining pressure increasing, the platform length gradually decreases, even disappears. In the stade I, the rigid effect of deep sandstone is remarkable. In the stage II, radial deformation of deep sandstone dominates. The transient strain of confining pressure compliance is defined, which shows three-stage evolution characteristics. In the stage III, the radial deformation is greater than the axial deformation in the pre-peak stage, but the opposite trend is observed in the post-peak stage. It is found that the dynamic permeability can be more accurately characterized by the radial strain. The relations between the permeability and stress−strain curves in various stages are revealed.

Key words: deep effect; stress−strain; platform; confining pressure effect; stress-seepage; permeability

Cite this article as: ZHANG Jun-wen, SONG Zhi-xiang, WANG Shan-yong. Mechanical behavior of deep sandstone under high stress-seepage coupling [J]. Journal of Central South University, 2021, 28(10): 3190−3206. DOI: https://doi.org/10.1007/s11771-021-4791-x.

1 Introduction

In-situ stress is a fundamental force causing rock deformation and damage during the excavation process of mining, tunnelling, and oil and gas exploration. Additionally, after excavation, the stress field is redistributed, which may also result in large deformation of surrounding rock [1−4]. With the increased mining of shallow coal resources, many mines in China will reach mining depths over 1000 m in the next 20 years [5, 6]. The deep coal resources at buried depths beyond a kilometre approximately total 2.95×10^{12} tons, which accounts for 53% of the total coal resources. At present, there are approximately 47 deep coal mines in China, such as Zhaogezhuang coal mine and Suncun coal mine, with mining depths of 1159 m and 1508 m, respectively [7−9]. In Suncun coal mine, the in-situ stress has reached 40−60 MPa at a mining depth of 1508 m, and the mine was continuously mined at a

Foundation item: Projects(51974319, 52034009) supported by the National Natural Science Foundation of China; Project(2020JCB01) supported by the China University of Mining and Technology (Beijing)
Received date: 2020-10-12; **Accepted date:** 2021-01-21
Corresponding author: SONG Zhi-xiang, PhD; Tel: +86-18810705970; E-mail: szxcumtb@126.com; ORCID: https://orcid.org/0000-0002-7797-5469

rate of 10 − 25 m/year [10], while the highest pore water pressure has been up to 10 MPa [11, 12]. In oil and gas engineering, the highest in-situ geo-stress can reach 200 MPa [13−15].

Various studies on the mechanical behavior of coal and rock have been conducted. Due to the great challenges in ground control in deep rock strata, substantial research efforts have been expended to reveal the mechanical behavior of deep-seated rocks for stability issues. ZHAO et al [16] studied the brittle-ductile transition characteristics and failure mechanism of Jinping marble by conducting the true triaxial compression test. TANG et al [17] obtained the progressive failure mechanism of rocks by conducting the triaxial compression test. ASADIZADEH et al [18] revealed the mechanical mechanism of jointed rock-like material subjected to uniaxial compression. MA et al [19] found that the elastic modulus of rock decreases exponentially with the number of loading cycles increasing. Moreover, the degradation of the elastic modulus is independent of the stress level and confining pressure. PELLET et al [20] investigated the mechanical behavior of gabbro under super-high confining pressures, up to 650 MPa, and argued that the mechanical degradation of porous rock was caused by the collapse of pores and grain displacement around original fractures. ZHANG et al [21] established the relationships among the permeability with the input energy, the dissipation energy and the elastic energy density of deep sandstone under three-stage loading and stress-seepage coupling. Some other results have also illustrated the mechanical behaviors of coal and rock under different conditions [22 − 34]. The findings reported in the above studies have made significant progress in understanding the mechanical behavior of coal and rock. Nevertheless, few studies have been performed on the original high in-situ stress state on mechanical behavior of deep sandstone. There is a need to better understand the effect of the original high in-situ stress state on the mechanical behavior of deep sandstone.

Besides, there is a significant correlation between the permeability and stress of coal and rock in deep geological environments. JIANG et al [35] proposed a damage model by stress-seepage coupling tests, thereby revealing the correlation among the permeability, microcrack density and crack opening degree. WANG et al [36] determined that the volumetric strain of sandstone links the seepage field to the stress field and is related to the permeability and fluid pressure. HU et al [37] studied the non-linear stress − strain relationship of saturated sandstone at various stress levels, the anisotropic characteristics of the Biot coefficient evolution law and the phenomenon of the significant increase in axial permeability when microcracks are initiated. XU et al [38] conducted short-term and creep triaxial compression tests on sandstone and revealed the permeability evolution behavior and failure mechanism of sandstone. A solid knowledge of the permeability and stress development of coal and rock is crucial for rational design and analysis of engineering stability. Nevertheless, few studies have been performed on the original high in-situ stress state on the mechanical behavior of coal and rock. Therefore, the permeability and stress development evolution behavior of deep sandstone is also worthy for further research.

In most of the studies mentioned above, the characteristics of the original high in-situ stress state of coal and rock in deep environments were neglected. Conventionally, the loading of mechanical tests starts from zero until macroscopic failure occurs. As shown in Figure 1, H is buried depth; σ_x, σ_y, σ_z are high initial in-situ stress in the x, y and z directions, respectively; $\sigma_{x'}$ is the minimum principal stress after unloading; $\sigma_{z'}$ is the maximum principal stress under axial loading. Firstly, the stress state of the deep roadway surrounding rock exhibits the initial high in-situ stress level before excavation. Secondly, the deep roadway is excavated because of engineering need, when the surrounding rock of deep roadway is subjected to the constant axial stress but the unloaded surrounding stress. Meanwhile, the axial loading on the surrounding rock of the deep roadway cannot be rapidly dissipated into deeper parts. As a result, the surrounding rock of deep roadway exhibits notable large deformation and even complete rupture characteristics due to the continuous axial loading. Therefore, a new method and concept of deep rock mechanics testing is proposed to reveal the mechanical behavior evolution law of the deep

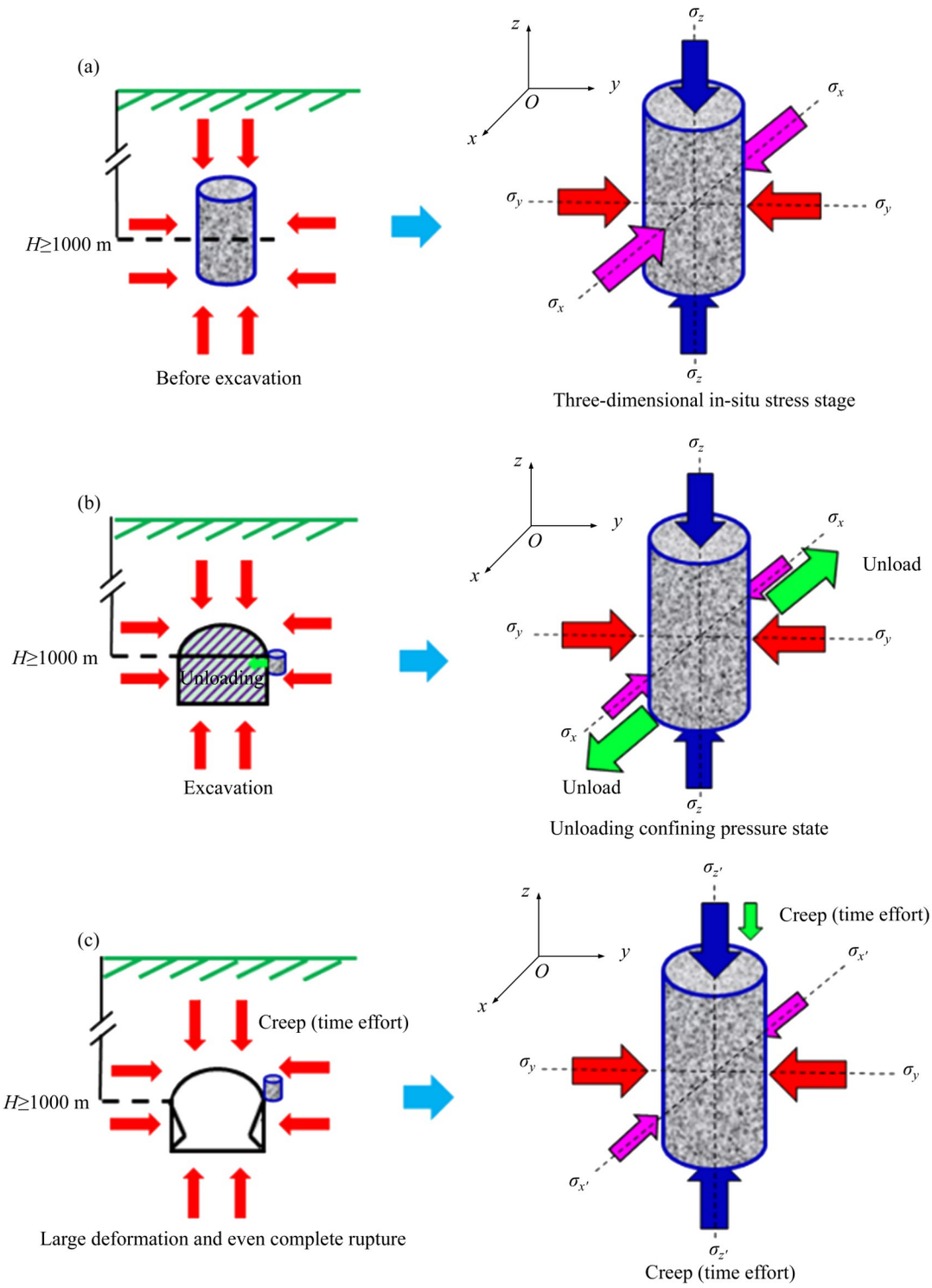

Figure 1 Corresponding engineering background for three-stage loading stress path: (a) High initial in-situ stress state reduction (stage I); (b) Constant axial pressure-unloading confining pressure (stage II); (c) Axial loading (stage III)

roadway surrounding rock after excavation at depths over 1000 m. Specifically, three-stage loading triaxial experiments of deep sandstone are conducted under high stress-seepage coupling. The stress path of the triaxial compression test is three-dimensional in-situ stress state reduction + the unloading effect + increasing axial loading (time effort). Therefore, the mechanical behavior evolution law of deep sandstone under high stress-seepage coupling is obtained. Additionally, this study provides ideas for obtaining the mechanical behavior of the deep surrounding rock.

2 Testing process and methods

2.1 Sampling site

Suncun coal mine is in Xintai, Shandong province, China. The roadway is excavated in the strata of sandstone. Besides, the deep sandstone was collected from the surrounding rock of the roadway in Suncun coal mine with a buried depth of 1150 m.

2.2 Sample preparation and basic parameter determination

The mineralogic composition of deep sandstone mainly includes feldspar, quartz and mica, and its appearance is grey-white. The deep sandstones were firstly cored in the field, and then cored sandstones were trimmed short and the two ends were lapped to form Φ25 mm×50 mm cylindrical specimens so that it can meet the standard of triaxial compression tests. The two ends and sides of deep sandstone were trimmed flattened to be an accuracy of ±0.05 mm. The deep sandstone was saturated in a vacuum pressure saturation device for 24 h before the tests. The whole preparation process was carried out at 25 °C. Additionaly, Poisson ratio, elastic modulus, and uniaxial compressive peak strength of the deep sandstone are 0.255, 11.572 GPa, and 62.65 MPa, respectively, based on the uniaxial compression testing (Figure 2). Moreover, it is observed that the whole uniaxial compression deformation process of deep sandstone undergoes five stages. Namely, stage 1 is the original microcrack compression stage; stage 2 is the linear elastic deformation stage; stage 3 denotes the stable crack expansion stage; stage 4 is the unstable crack expansion stage; and stage 5 is the post-peak strain softening stage.

2.3 Test set-up

The triaxial tests were conducted using GCTS multi-field coupled servo system. The system mainly consists of an RIR-1500 triaxial loading system, confining and pore pressure boosters, a hydraulic station, a sonic excitation acquisition system, a acoustic emission meter, and a data acquisition and control system. The RIR-1500 triaxial loading system can apply a maximum axial load of 1500 kN, a maximum confining pressure of 140 MPa, a maximum pore pressure of 140 MPa and a maximum temperature of 200 °C [39].

2.4 Permeability test principle under high stress-seepage coupling

As shown in Figure 3, where P is the axial loading; P_1 is the pressure of injected CO_2; P_2 is the outlet pressure and P_c is the confining pressure. The detailed explanation and description of the specific permeability test principle under high stress-seepage coupling according to Ref. [21].

2.5 Stress path

To obtain the mechanical behavior evolution law of deep sandstone under high stress-seepage coupling, the stress state of the surrounding rock of deep roadway is simulated at a depth over 1000 m during the whole excavation process. Three-stage loading is conducted under high stress-seepage coupling and confining pressures of 6, 13, 20 and 23 MPa. The corresponding three-stage loading stress path is shown in Figure 4. The specific steps are as

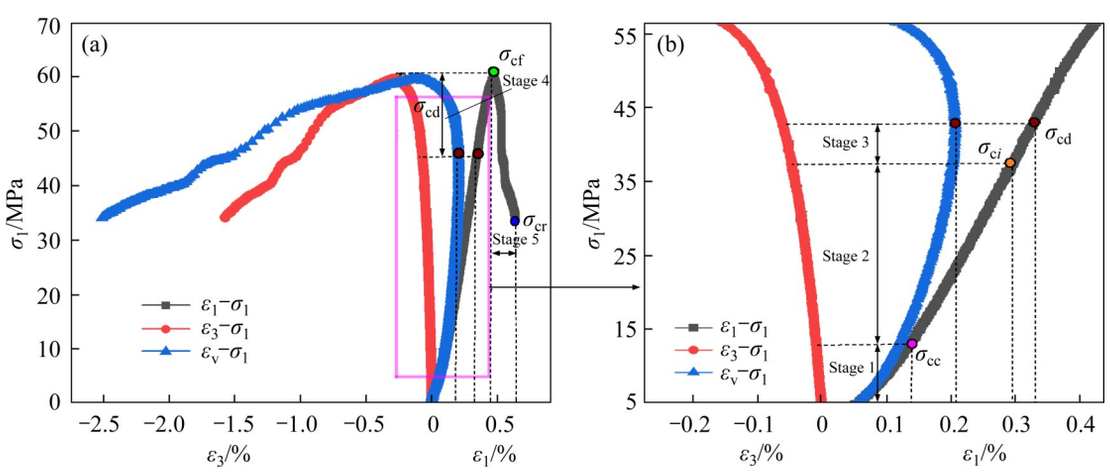

Figure 2 Stress−strain curve of deep sandstone obtained by uniaxial compression test

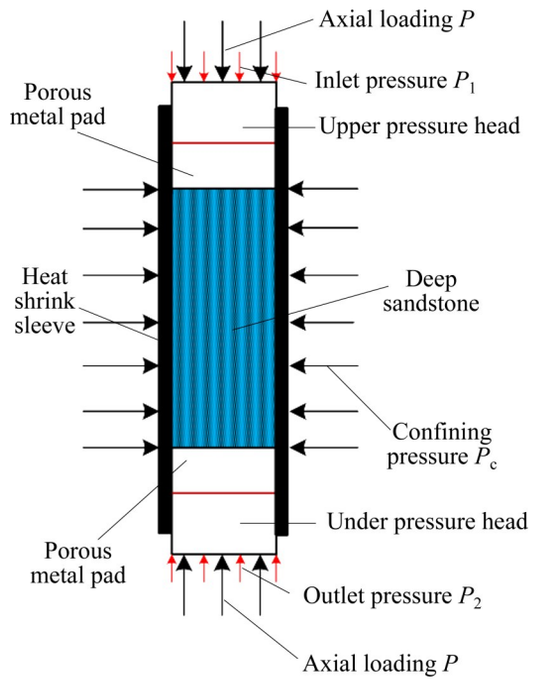

Figure 3 Principle of permeability test for deep sandstone

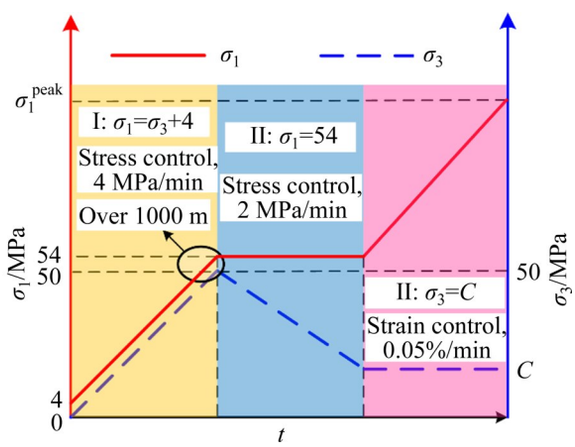

Figure 4 Three-stage loading stress path

follows:

1) High initial in-situ stress state reduction (stage I): In this stage, the loading process of deep sandstone is controlled by the stress mode, and the deviatoric stress is maintained at 4 MPa. The deep sandstone is loaded to the three-dimensional hydrostatic state (axial load σ_1=54 MPa, and confining pressure σ_3=50 MPa) [12, 40, 41] at a loading rate of 4 MPa/min for σ_1 and σ_3. The triaxial testing system automatically records the relevant data during the loading process.

2) Constant axial pressure-unloading confining pressure (stage II): After stage I, σ_3 is unloaded at a rate of 2 MPa/min (for safety) to the corresponding design values of 6, 13, 20 and 23 MPa, while keeping the axial stress constant.

During the unloading process, the stress control model is maintained, and the permeability of deep sandstone is measured by the transient differential pressure decay method every 10 MPa during the unloading process, and the relevant data are automatically recorded.

3) Axial loading (stage III): After stage II, the loading control mode is switched to the strain control mode with a strain rate of 0.05%/min. Axial loading is increased from σ_1=54 MPa until the deep sandstone enters the post-peak strain softening stage while the confining pressure is kept constant. The permeability of deep sandstone is measured every 10 MPa during the loading process, and the testing system automatically records the relevant data.

3 Results and analyses

3.1 Stress–strain curve of deep sandstone during three-stage loading process

As shown in Figure 5, the stress–strain curve of deep sandstone could be divided into three stages: the high initial in-situ stress state reduction stage I, the constant axial pressure-unloading confining pressure stage II, and the axial loading stage III.

In stage I, both the initial axial and radial strains of each deep sandstone are positive as they are integrally compressed under triaxial pressure conditions. For instance, when the deep sandstone is subjected to a confining pressure of 6 MPa, the axial strains increased from 0 to 0.35%, and the radial strains increased from 0 to 0.33%. A similar evolution law could be observed for both the axial and radial strains of the other deep sandstone.

In stage II, the axial pressure is maintained at 54 MPa while unloading the confining pressure to different degrees. A platform of different lengths is observed in the stress–strain curves. The platform phenomenon is mainly attributed to the effect of stage I, during which the initial fissures of deep sandstone are compacted or closed. The deep sandstone under low confining pressures can be unloaded with a larger amount of deformation in stage II. The radial inhibitory effect decreased notably, leading to significant radial expansion of deep sandstone. Therefore, a long radial platform

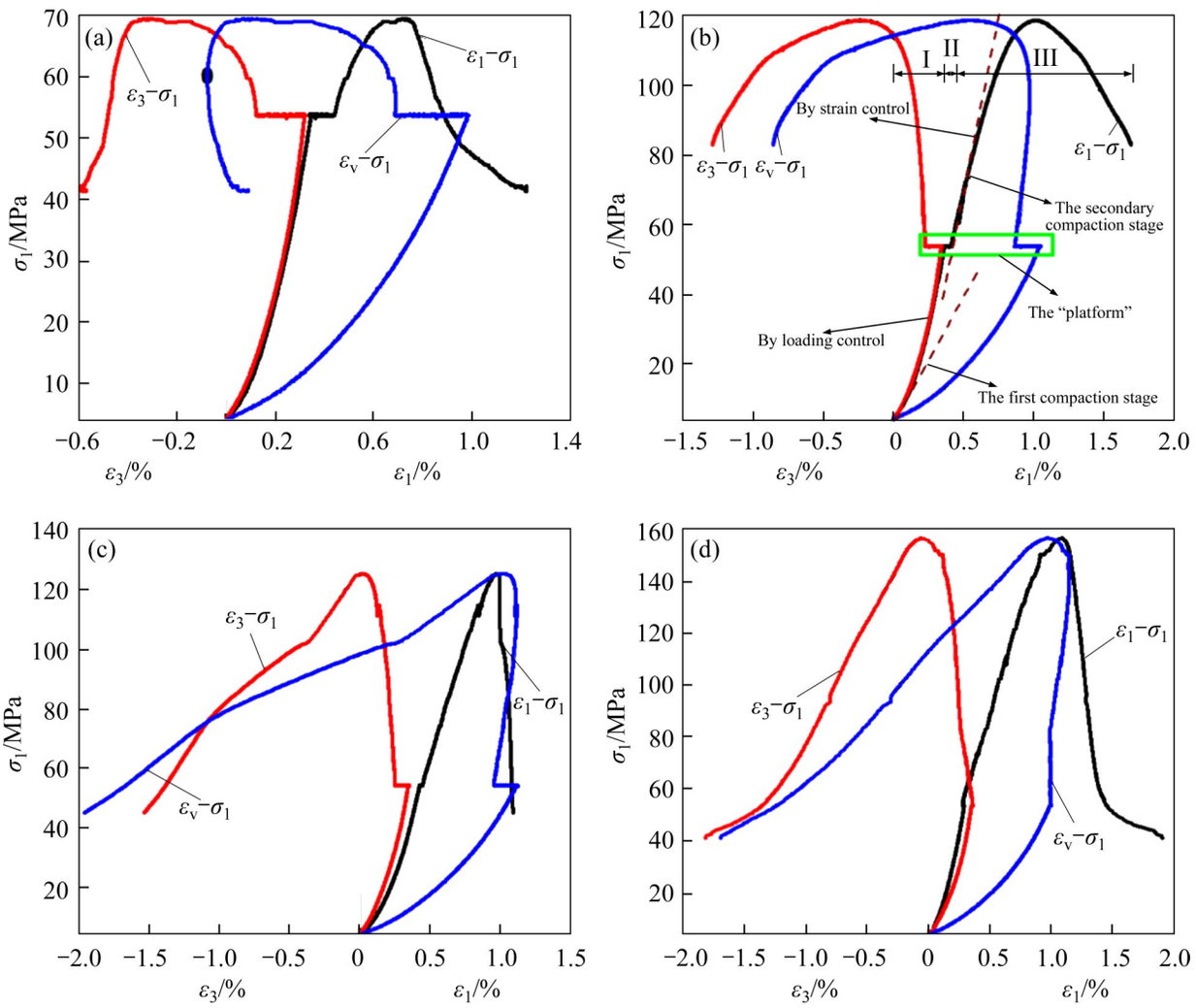

Figure 5 Stress–strain curves for three-stage loading of deep sandstone under different confining pressures: (a) σ_3= 6 MPa; (b) σ_3=13 MPa; (c) σ_3=20 MPa; (d) σ_3=23 MPa

occurred. According to the strength theory of Griffith [42–44], unloading the confining pressure reopens many compacted or closed fissures within deep sandstone, or initiated many new fissures, which even drastically increase. A highly concentrated tensile stress can easily develop around fissures with an increased aperture. As a result, with increasing axial strain, produced a significant platform shape occurs along the axial direction. The platform phenomenon of the volumetric strain indicates that radial deformation of deep sandstone is dominant in stage II, while axial deformation is only an associated phenomenon of radial deformation. In stage II, the confining pressure is unloaded to a low degree, and the radial inhibitory effect is not distinct. Therefore, radial expansion is insignificant, which makes it difficult to form a radial platform. Accordingly, the apparent platform of the axial strain hardly develops.

In stage III, axial loading started from the initial high in-situ stress state, including five stages, i.e., the microcrack compaction stage, linear elastic deformation stage, stable crack growth stage, accelerated crack growth stage and post-peak strain softening stage, which exhibit differences and similarities relative to the deformation characteristics of conventional triaxial loading. These similarities indicate that a memory effect occurs in rock deformation [45]. These differences are mainly that the degree of hardening is notably higher than that of the conventional triaxial loading process. The microcrack compaction stage denotes the secondary compaction stage of the new cracks developed in stage II and that of the original internal

micropores. This stage is notably different from the formation mechanism of the initial microcracks in the stress − strain curves of conventional triaxial loading.

3.2 Deformation characteristics of deep sandstone under three-stage loading

3.2.1 High initial in-situ stress state reduction stage

To characterize the deformation sensitivity of each deep sandstone in stage I, a compression sensitivity coefficient η is introduced. The compression sensitivity coefficient η is defined as the ratio of the strain increase to the previous strain, which is recorded by the triaxial system in stage I:

$$\eta_j = \frac{\varepsilon_j^{i+1} - \varepsilon_j^i}{\varepsilon_j^i} \tag{1}$$

where j=1, 3, v; η_1, η_3 and η_v are the axial, radial and volumetric compression sensitivity coefficients, respectively; ε_1^i, ε_3^i and ε_v^i are the i-th axial, radial and volumetric strains, respectively.

Figure 6 shows that under 13 MPa, η_1 decreased from 3.78 to 0.0017; η_3 decreased from 0.456 to 0.0032; η_v decreased from 0.693 to 0.0027. The axial, radial and volumetric compression sensitivity coefficients of other deep sandstone also show similar trends, tending to be a 0-scale "hardening line", which indicates that the deep sandstone exhibits significant compression effects in a high-stress environment, and the high initial in-situ stress state reduction effect is notable. The deep sandstone is greatly compacted due to closure of the initial micropores. Therefore, the rigid effect is remarkable after the high initial in-situ stress state reduction stage, where the rock is very similar to a rigid body.

3.2.2 Constant axial pressure-unloading confining pressure stage

In most previous studies, the mechanical behavior of coal and rock in the unloading confining pressure stage is better characterized by Poisson ratio, unloading ratio [46], uniform confining pressure drop parameters [47], lateral expansion coefficient [48], and strain of confining pressure compliance [49 − 51]. The mechanical behavior of coal and rock in the unloading confining pressure stage can be revealed better with these parameters.

GOWD et al [49], ALAM et al [50] and SUKPLUM et al [51] have defined the strain of confining pressure compliance for rock samples, but it cannot reflect the gradient response characteristics of stress and deformation during the entire unloading confining pressure process. To further clarify the progressive deformation response behavior of deep sandstone in the constant axial pressure-unloading confining pressure stage, the

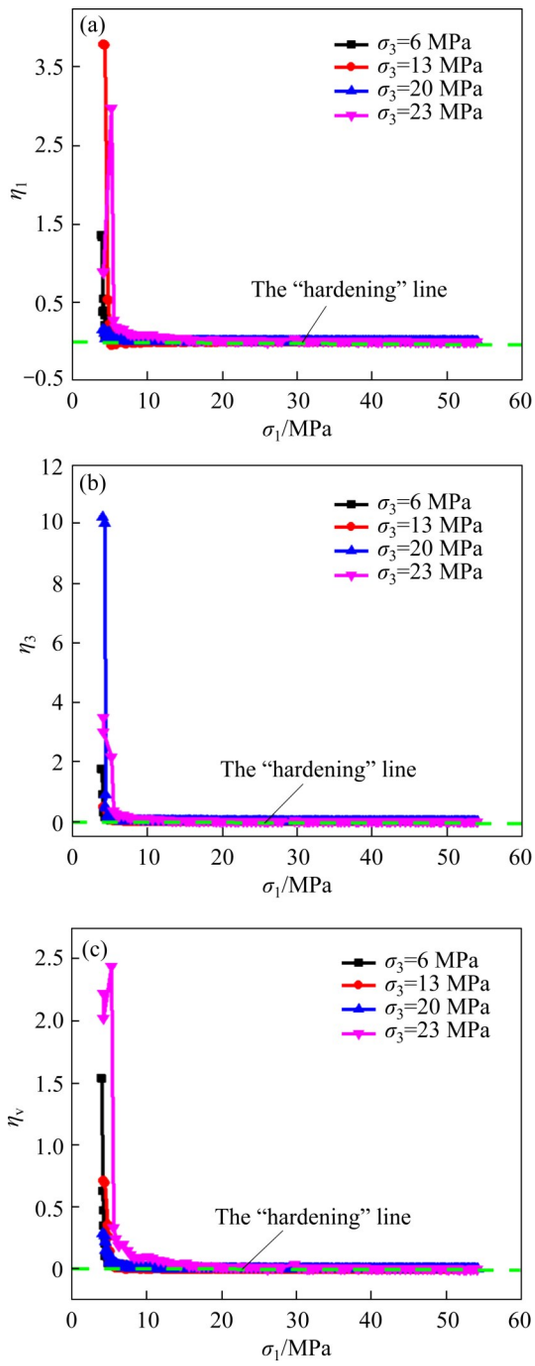

Figure 6 Curves of compression sensitivity coefficient of deep sandstone in initial high in-situ stress state reduction stage: (a) η_1; (b) η_3; (c) η_v

axial and radial transient strains of confining pressure compliance ξ_1 and ξ_3 are respectively proposed as the ratio of the k-th axial and radial strain increments $\Delta\varepsilon_1^k$, $\Delta\varepsilon_3^k$ between the starting point of the unloading confining pressure and the unloading point recorded by the triaxial system during the unloading process to the corresponding confining pressure unloading amount $\Delta\sigma_3^k$:

$$\xi_1 = \frac{\Delta\varepsilon_1^k}{\Delta\sigma_3^k},\ \xi_3 = \frac{\Delta\varepsilon_3^k}{\Delta\sigma_3^k} \tag{2}$$

$$\Delta\varepsilon_1^k = \varepsilon_1^k - \varepsilon_1^0,\ \Delta\varepsilon_3^k = \varepsilon_3^k - \varepsilon_3^0 \tag{3}$$

$$\Delta\sigma_3^k = \sigma_3^k - \sigma_3^0 \tag{4}$$

where σ_3^k and σ_3^0 are the k-th and the initial confining pressures in the stage II, respectively; ε_1^k, ε_3^k are the k-th axial and radial strains in the stage II, respectively; and ε_1^0, ε_3^0 are the initial axial strain and the initial radial strain in the stage II, respectively.

The transient strain of confining pressure compliance ξ_i can reflect the influence on the progressive deformation of deep sandstone better under various confining pressures. The higher the transient strain of confining pressure compliance is, the more significant the unloading effect on deep sandstone along the stress unloading direction is. This also indicates that deformation of deep sandstone dominates along this direction. According to the data recorded by the triaxial system and Eqs. (2) − (4), the axial and radial transient strain curves of the confining pressure compliance of deep sandstone under the various confining pressures are obtained, as shown in Figures 7 and 8.

The axial and radial transient strain curves of the confining pressure compliance exhibit obvious three-stage evolution characteristics (Figures 7 and 8). The axial transient strain curves of the confining pressure compliance can be divided into the sudden drop phase (I), stable development phase (II) and accelerated increase phase (III). The radial transient strain curves of the confining pressure compliance can be divided into the rapid increase phase (I),

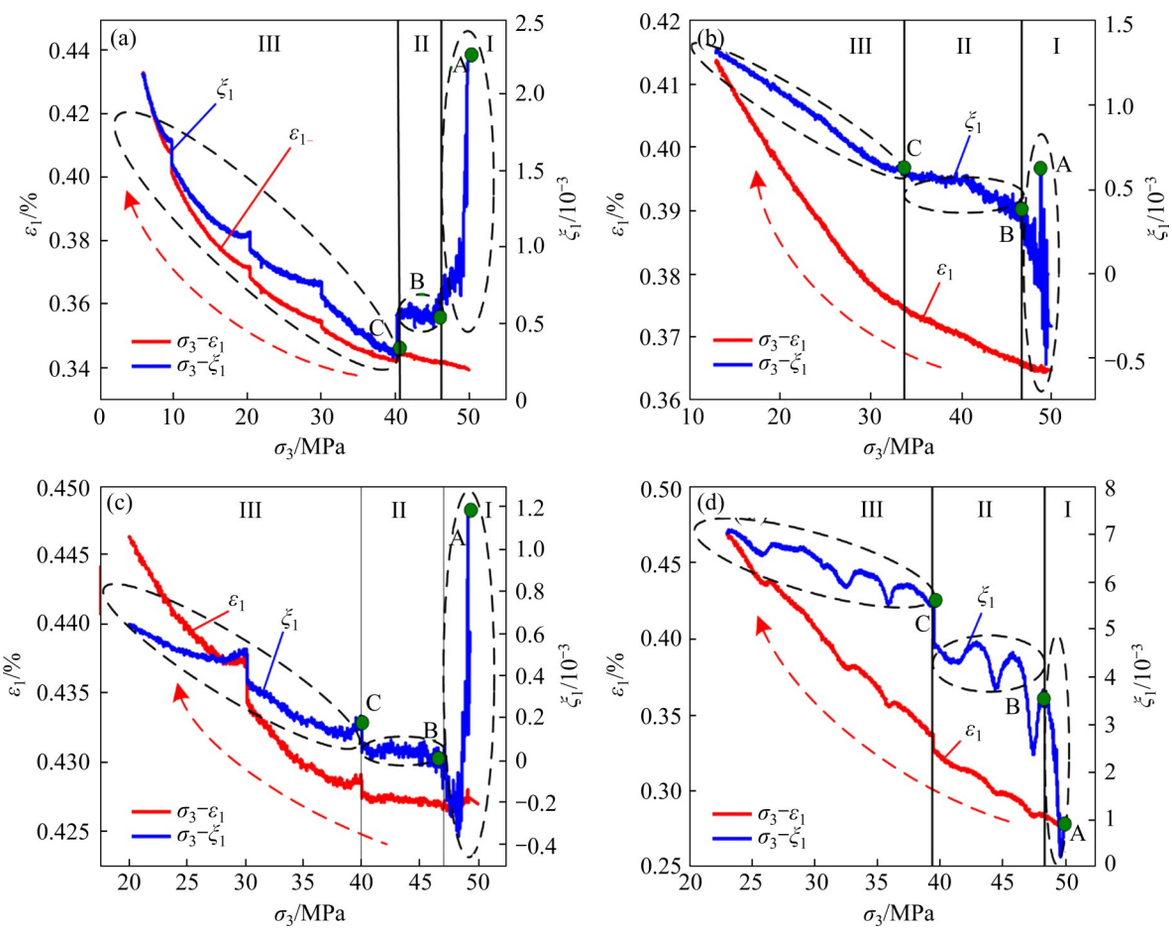

Figure 7 Axial transient strain curves of confining pressure compliance under different confining pressures: (a) σ_3= 6 MPa; (b) σ_3=13 MPa; (c) σ_3=20 MPa; (d) σ_3=23 MPa

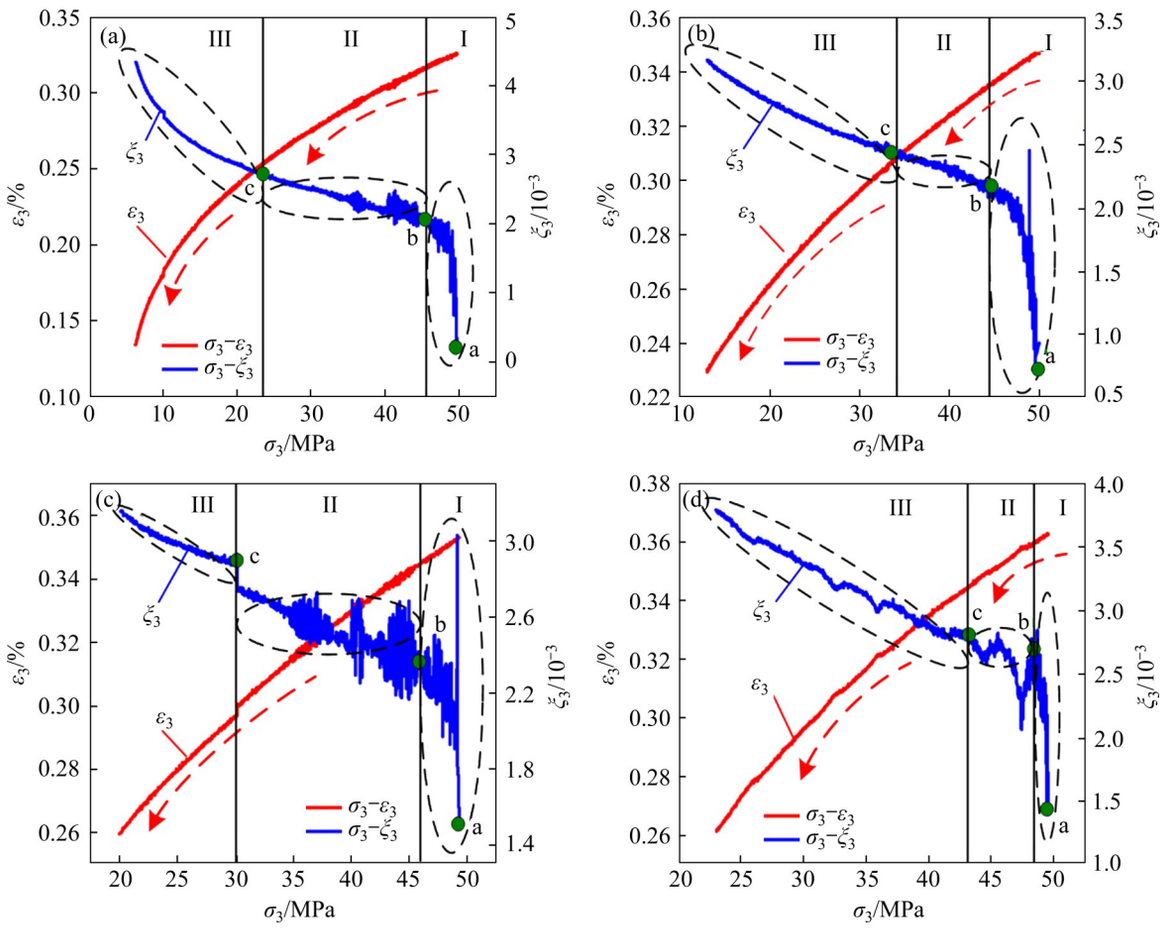

Figure 8 Radial transient strain curves of confining pressure compliance under different confining pressures: (a) σ_3= 6 MPa; (b) σ_3=13 MPa; (c) σ_3=20 MPa; (d) σ_3=23 MPa

stable development phase (II) and accelerated increase phase (III). Among them, points A, B and C are the demarcation points of each phase of the axial transient strain curve of the confining pressure compliance, respectively, and points a, b, and c are the demarcation points of each phase of the radial transient strain curve of the confining pressure compliance, respectively. There is a significant drop in the axial transient strain curves of the confining pressure compliance in phase I. The reason for this significant difference may be that deep sandstone has accumulated a large amount of elastic energy after undergoing the high initial in-situ stress state reduction stage. When the constant axial pressure-unloading confining pressure stage is reached, the elastic energy is rapidly released along the radial direction. The radial inhibition of deep sandstone is significantly weakened; the radial deformation space has been greatly extended; and the deformation capacity is increased. Radial deformation simultaneously produces fractures with increased openings, and the tensile stress formed at the sample ends acts on the axial direction of deep sandstone to inhibit axial deformation. As a result, axial deformation is not fully reflected, which leads to a significant difference in phase I of the axial and radial transient strain curve of confining pressure compliance.

In phase II, ξ_1 and ξ_3 undergo stable development changes. The reason for this phenomenon may be due to the occurrence of time effect [52, 53], which causes the release rate of energy in phase II to gradually decrease, and the axial and radial inhibition effects of deep sandstone in this phase are weakened. Therefore, the axial and radial transient strain curves of confining pressure compliance exhibit a steady development trend.

In phase III, the overall stiffness of deep sandstone is significantly reduced due to the

cumulative effect of stages I and II. In the later unloading confining pressure stage, the combination of axial compression and radial inhibition weakening resulted in large deformation of deep sandstone, causing the axial and radial transient strain curves of confining pressure compliance to exhibit the phenomenon observed in phase III. On the whole, it is found that the radial transient strain of confining pressure compliance increment $\Delta\xi_3$ in each phase is larger than the axial transient strain of confining pressure compliance increment $\Delta\xi_1$, which indicates that radial deformation of deep sandstone dominates in the constant axial pressure-unloading confining pressure stage. Additionaly, the axial transient strain curves of confining pressure compliance and the axial strain curves exhibited a co-directional confluence trend, while the radial transient strain curves of confining pressure compliance and the radial strain curves showed a reverse shunt trend.

Comparing the axial and radial transient strain curves of confining pressure compliance under the confining pressures of 6, 13, 20 MPa, a certain difference is observed between the axial and radial transient strain curves of confining pressure compliance under a confining pressure of 23 MPa. This may be due to an operational error (pressure rod instability) in the test [54, 55], which resulted in ξ_{3max} under this confining pressure greatly deviating from ξ_{3max} under the other confining pressures (ξ_{3max} is the maximum radial transient strain of confining pressure compliance). However, the overall variation trends of the axial and radial transient strain curves of confining pressure compliance are consistent.

3.2.3 Axial loading stage

As shown in Figure 9, the initial axial stress in this stage is 54 MPa. MENG et al [56] introduced the sensitivity coefficient of permeability to obtain the average pore pressure by using the derivative of the permeability to the pore pressure, which suitably characterized the sensitivity evolution characteristics of the permeability relative to the average pore pressure of low-permeability

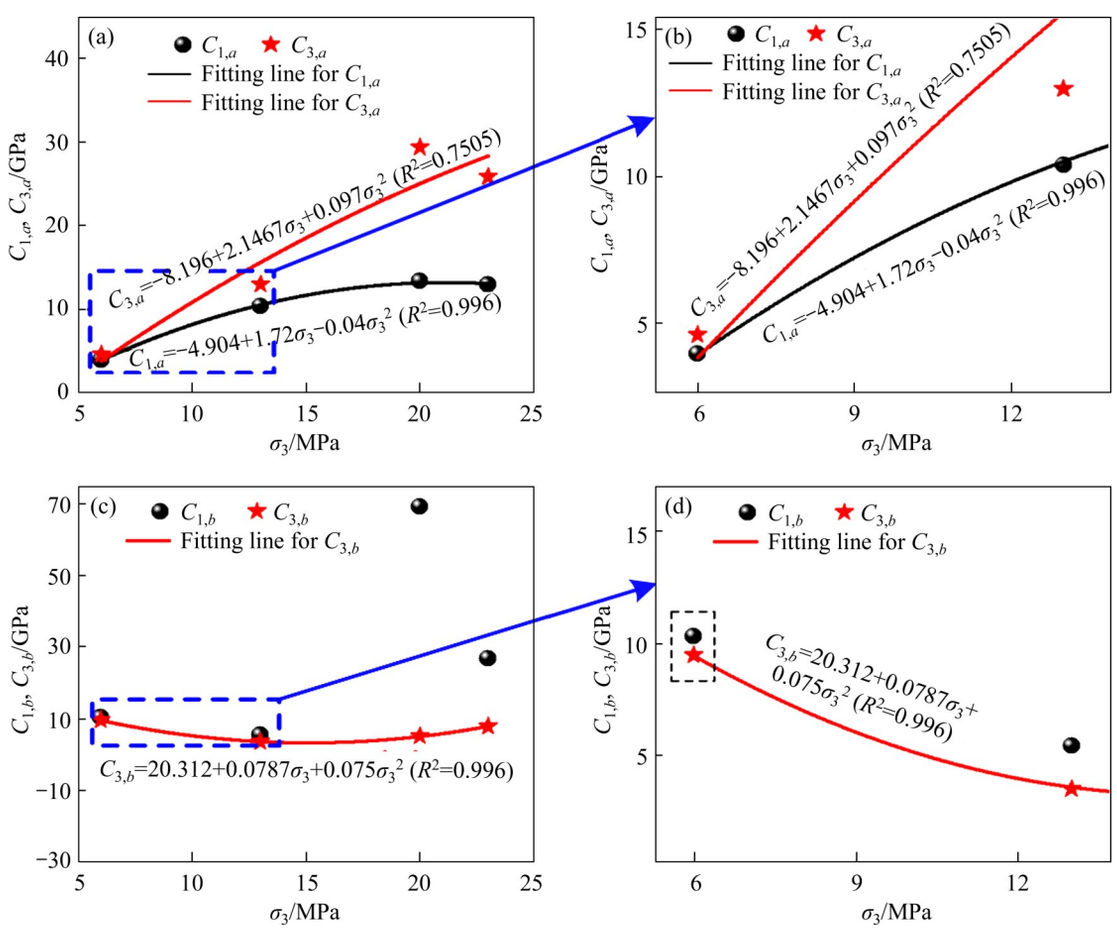

Figure 9 Axial and radial deformation sensitivity for deep sand stone of: (a, b) Pre-peak; (c, d) Post-peak

sandstones under various confining pressures. Therefore, the slope of the stress − strain curve is used as a deformation sensitivity indicator to characterize the prominent deformation difference between the pre- and post-peak stages. To simplify the calculation, the axial and radial pre- and post-peak deformation sensitivity is defined as follows:

$$\begin{cases} C_{i,a} = \dfrac{\sigma_{1\max} - \sigma_{10}}{\left|\varepsilon_{i\max} - \varepsilon_{i0}^{a}\right|} \\ C_{i,b} = \dfrac{\sigma_{1\max} - \sigma_{10}}{\left|\varepsilon_{i\max} - \varepsilon_{i0}^{b}\right|} \end{cases} (i = 1, 3) \tag{5}$$

where $C_{i,a}$ and $C_{i,b}$ represent the deformation sensitivity of the pre- and post-peak, respectively (i=1 and 3 represent the axial and radial strains, respectively). $\sigma_{1\max}$ and $\varepsilon_{i\max}$ represent the axial and radial strain corresponding to the peak strength, respectively. σ_{10}=54 MPa, ε_{i0}^{a} and ε_{i0}^{b} are the axial and radial strains corresponding to the pre- and post-peak staring strength σ_{10}, respectively.

As shown in Figure 9(a), the radial deformation sensitivity of the pre-peak stage is significantly higher than the axial deformation sensitivity under various confining pressures conditions, which means that the radial deformation is greater than the axial deformation in the pre-peak stage, but the opposite trend is observed in the post-peak stage according to the trends of the axial and radial deformation sensitivity of the post-peak stage in Figure 9(b). This indicates that the radial deformation of deep sandstone in the post-peak stage lagging behind the axial deformation, but the opposite deformation law of deep sandstone in the pre-peak stage is better characterized. Additionaly, the axial and radial deformation sensitivity of the pre- and post-peak stage of deep sandstone demonstrated a strong non-linear function relationship with the confining pressures. The corresponding functional expressions are as follows:

$$\begin{cases} C_{1,a} = -4.094 + 1.72\sigma_3 - 0.04\sigma_3^2,\ R^2 = 0.996 \\ C_{3,a} = -8.196 + 2.1476\sigma_3 + 0.097\sigma_3^2,\ R^2 = 0.7505 \\ C_{3,b} = 20.312 + 0.0787\sigma_3 + 0.075\sigma_3^2,\ R^2 = 0.996 \end{cases} \tag{6}$$

3.3 Permeability evolution

3.3.1 Determination of strength demarcation point

Self-similarity characteristics are observed in the deformation of each deep sandstone along the same loading path. Hence, the stress−strain curve of deep sandstone with three-stage loading under a confining pressure of 13 MPa is only presented to determine each strength demarcation point. Methods that could determine the crack closure stress σ_{cc} and crack initiation stress σ_{ci} from the stress − strain curves of coal and rock have been previously reported in Refs. [57 − 60]. Therefore, the crack closure stress σ_{cc} and crack initiation stress σ_{ci} are determined according to Ref. [57], and then the strength demarcation point of each deep sandstone under the various confining pressures is obtained. Figure 10 shows the method of determining the strength demarcation point. In Figure 10, σ_{cd} is the stress corresponding to the maximum volumetric

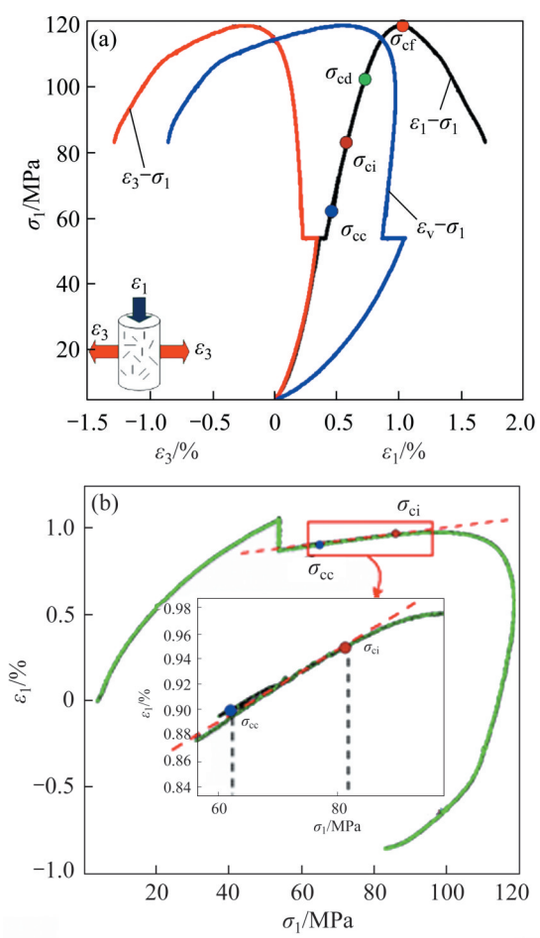

Figure 10 Diagram of each strength demarcation point of three-stage loading curves of deep sandstone under confining pressure of 13 MPa: (a) Three-stage loading stress − strain curves; (b) Axial stress − volumetric strain curve

strain rate; and σ_{cf} is the peak strength; σ_{cc} is the crack closure stress during the second compaction stage; σ_{ci} is the crack initiation stress.

3.3.2 Corresponding stage characteristic of stress − strain and permeability curves

Under external loading, the deformation of coal and rock has self-similarity characteristics [19, 61 − 63], which can result in the permeability evolution including the self-similarity characteristics. For this reason, the stress−strain and permeability evolution curves of deep sandstone in the three-stage loading process under a confining pressure of 13 MPa are used for analysis.

As shown in Figure 11, in stage I, the internal original micropores in the deep sandstone are compacted, and the axial and radial stiffness are close to that of a perfectly elastic body. As a result, the opening of the original axial and radial microcracks decreased dramatically, and thus many original seepage channels become narrower. At the end of this stage, the permeability of deep sandstone

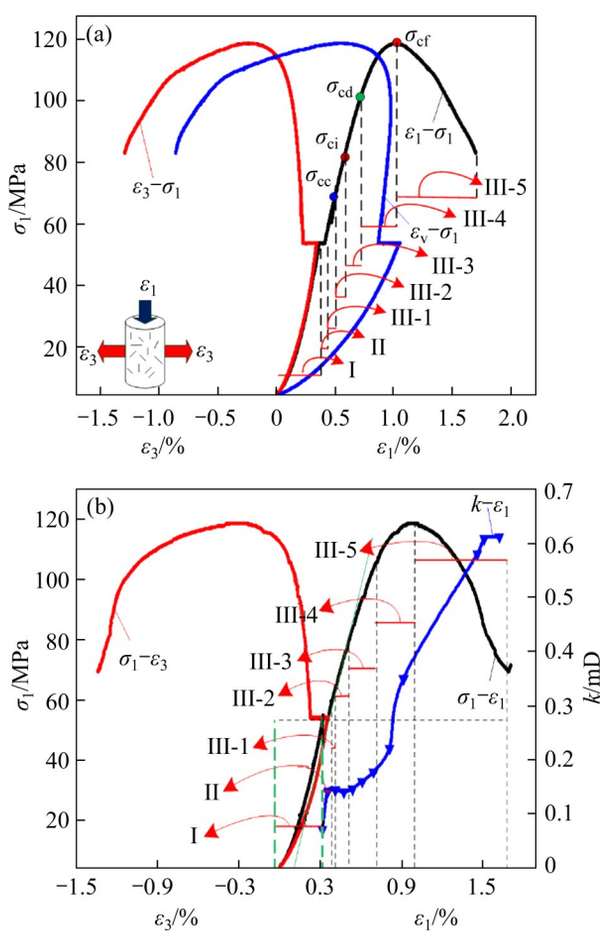

Figure 11 (a) Stress − strain curves and (b) permeability curves during entire deformation process of deep sandstone under a confining pressure of 13 MPa

was reduced to 0.0737 mD. In stage II, radial deformation of deep sandstone expanded due to the weakening effect of the confining pressure through unloading, leading to an increase in the radial crack opening. As a result, the seepage channel width increased with increasing permeability from 0.0737 to 0.14435 mD. Stage III can be divided into five substages, i. e., III-1 is the microcrack secondary compaction stage; III-2 is the linear elastic deformation stage; III-3 is the steady growth stage of new cracks; III-4 is the accelerated crack growth stage; III-5 is the post-peak strain softening stage. In stage III-1, the deep sandstone was compacted again, causing the opening of pores and cracks to decrease again. Therefore, the seepage channels again narrowed. This resulted in a slight decrease in permeability from 0.14435 to 0.14435 mD. In stage III-2, due to the dynamic balance evolution between the external and internal fields, the internal stress of deep sandstone is in a state of dynamic balance. Therefore, the internal crack opening level of deep sandstone remains basically unchanged. In other words, the width of the seepage channels remains basically unchanged. This is the reason that the permeability of deep sandstone is basically constant. In stage III-3, the permeability increased from 0.16255 to 0.1801 mD. This is mainly because many new micro-cracks are generated in this stage, thereby intensifying seepage channels and slightly rising the permeability of deep sandstone. In stage III-4, the permeability greatly increased from 0.1801 to 0.4025 mD. This is mainly because when the peak stress was reached, macro-fractures began to develop within the deep sandstone, and large seepage channels were formed, leading to a sharp increase in permeability. In stage III-5, connected macro-cracks were produced in the deep sandstone, and gas flowed through the connected macro-cracks. As the amount of friction energy dissipation during gas seepage is relatively small, the pressure energy drop of the gas flow is limited. Therefore, the seepage flow and permeability in this stage were stable or only slightly decreased.

In summary, there is a good consistency between the permeability evolution and stress−strain curve characteristics during the entire deformation process of deep sandstone. Meanwhile, the peak permeability point of deep sandstone notably lags

behind the peak stress point, which may be caused by the characteristics of itself [36].

3.3.3 Permeability sensitivity analysis

Using the absolute radial strain, WANG et al [36] plotted axial strain−permeability and absolute radial strain−permeability curves and reported that the radial strain could accurately characterize the permeability evolution characteristics of rocks. Due to space limitations, this paper selected the permeability evolution curve of the three-stage loading process of deep sandstone under a confining pressure of 13 MPa. The permeability-axial strain curve has the same evolution trend as the permeability−radial strain curve (Figure 12), but the radial deformation sensitivity of deep sandstone is significantly higher than the axial deformation sensitivity in the pre-peak stress stage, and radial deformation is significantly ahead of axial deformation. This indirectly reflects that the radial strain can more accurately characterize the permeability variation of deep sandstone compared to the axial strain. Among the various stages, in stage I, the deep sandstone is compressed in three directions, and the compression effect is remarkable. At this moment, the axial and radial stiffness resemble those of an elastic body. According to the strength theory of Griffith [42−44], unloading the confining pressure weakened the radial inhibition effect in stage II. This led to previously compacted cracks to re-open. Tensile stress develops around cracks with an increased aperture, and the highly concentrated stress causes the deep sandstone to be deformed axially, causing axial compression as well as an increase in the axial strain. This intensifies the axial stiffness of deep sandstone. Therefore, after the deep sandstone core enters to stage III, the radial deformation sensitivity is significantly higher than the axial deformation sensitivity, and pre-peak radial deformation then leads to the occurrence of axial deformation. In addition, the axial, radial and volumetric strains of deep sandstone demonstrated a strong linear function relationship with the permeability. The corresponding functional expressions are as follows:

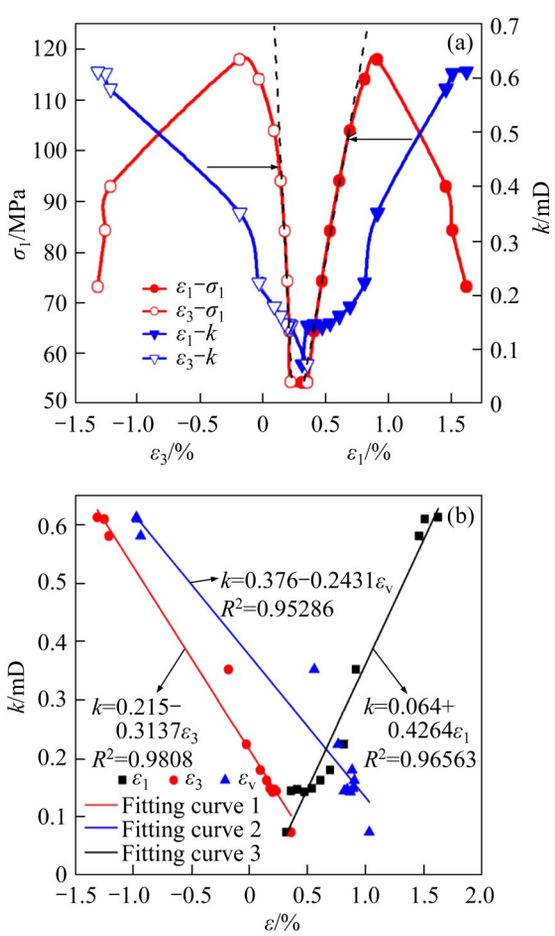

Figure 12 Sensitivity analysis curves of strain characterizing permeability: (a) Permeability − strain evolution curves; (b) Permeability − strain function relationships

$$\begin{cases} k = -0.064 + 0.4264\varepsilon_1,\ R^2 = 0.96563 \\ k = 0.215 - 0.3137\varepsilon_3,\ R^2 = 0.9808 \\ k = 0.376 - 0.2431\varepsilon_v,\ R^2 = 0.95286 \end{cases} \quad (7)$$

From the best-fit correlation coefficients, the dynamic change in permeability can be most accurately characterized by the radial strain.

4 Conclusions

1) The mechanical behavior of deep sandstone under high stress-seepage coupling is investigated using a GCTS multi-field coupled servo system. The stress−strain curve of the deep sandstone during the three-stage loading process under high stress-seepage coupling is obtained, including stress−strain curves exhibiting platform of various lengths and secondary compaction phenomena.

2) In the constant axial pressure-unloading confining pressure stage, the transient strain of confining pressure compliance is defined, and its axial and radial curves show obvious three-stage evolution characteristics. Additionaly, the mechanical behavior mechanism of the radial

deformation of deep sandstone in this stage is revealed. In the axial loading stage, the radial deformation is greater than the axial deformation in the pre-peak stage, but the opposite trend is observed in the post-peak stage.

3) Corresponding to the stress − strain curves, the permeability increases from the lowest value to the second stage, and the third stage illustrates a change trend from a slight decreasing, basically constant, slowly rising, sharp transition rising to basically constant or slightly decreasing in sequence. According to the permeability-strain curve and its functional relationship analysis, the radial strain of deep sandstone can more accurately characterize the permeability evolution compared to the axial strain.

However, the new method and concept proposed in this paper still have limitations, such as neglecting the significant differences between the various geological conditions of the samples. The evolution law of the mechanical behaviour will be more consistent with the mechanical behaviour under the corresponding mine sampling geological conditions compared to that in conventional triaxial loading. Therefore, this study can provide basic theoretical support for stability control of actual deep mine engineering roadways.

Contributors

ZHANG Jun-wen provided the concept, idea and supervision of manuscript, gave the funding acquisition and provided the resources for the manuscript. SONG Zhi-xiang conducted the literature review, wrote the first draft of the manuscript and edited the draft of manuscript. WANG Shan-yong provided the re-supervision of manuscript.

Conflict of interest

ZHANG Jun-wen, SONG Zhi-xiang, and WANG Shan-yong declare that they have no conflict of interest.

References

[1] STEINER W. Tunnelling in squeezing rocks: Case histories [J]. Rock Mechanics and Rock Engineering, 1996, 29(4): 211−246. DOI: 10.1007/BF01042534.

[2] DALGıÇ S. Tunneling in squeezing rock, the Bolu tunnel, Anatolian Motorway, Turkey [J]. Engineering Geology, 2002, 67(1, 2): 73 − 96. DOI: 10.1016/S0013-7952(02)00146-1.

[3] XIE He-ping, GAO Feng, JU Yang. Research and development of rock mechanics in deep ground engineering [J]. Chinese Journal of Rock Mechanics and Engineering, 2015, 34 (11): 2161−2178. (in Chinese)

[4] YANG Sheng-qi, CHEN Miao, JING Hong-wen, CHEN Kun-fu, MENG Bo. A case study on large deformation failure mechanism of deep soft rock roadway in Xin'an coal mine, China [J]. Engineering Geology, 2017, 217: 89 − 101. DOI: 10.1016/j.enggeo.2016.12.012.

[5] LI T, CAI M F, CAI M. A review of mining-induced seismicity in China [J]. International Journal of Rock Mechanics and Mining Sciences, 2007, 44(8): 1149 − 1171. DOI: 10.1016/ j.ijrmms.2007.06.002.

[6] ZHU Shu-yun, JIANG Zhen-quan, ZHOU Kai-jun, PENG Guang-qing, YANG Chao-wei. The characteristics of deformation and failure of coal seam floor due to mining in Xinmi coal field in China [J]. Bulletin of Engineering Geology and the Environment, 2014, 73(4): 1151 − 1163. DOI: 10.1007/s10064-014-0612-x.

[7] ZHANG Qin-li, HU Guan-yu, WANG Xin-min. Hydraulic calculation of gravity transportation pipeline system for backfill slurry [J]. Journal of Central South University of Technology, 2008, 15(5): 645 − 649. DOI: 10.1007/s11771-008-0120-x.

[8] SHEN Bao-tang. Coal mine roadway stability in soft rock: A case study [J]. Rock Mechanics and Rock Engineering, 2014, 47(6): 2225−2238. DOI: 10.1007/s00603-013-0528-y.

[9] ZHANG Kai, ZHANG Gui-min, HOU Rong-bin, WU Yu, ZHOU Hong-qi. Stress evolution in roadway rock bolts during mining in a fully mechanized longwall face, and an evaluation of rock bolt support design [J]. Rock Mechanics and Rock Engineering, 2015, 48(1): 333−344. DOI: 10.1007/s00603-014-0546-4.

[10] HE Man-chao, XIE He-ping, PENG Su-ping, JIANG Yao-dong. Study on rock mechanics in deep mining engineering [J]. Chinese Journal of Rock Mechanics and Engineering, 2005, 24(16): 2803−2813. (in Chinese)

[11] GRAHAM J, SAADAT F, GRAY M N. High-pressure triaxial testing on the Canadian reference buffer material [J]. Engineering Geology, 1990, 28(3, 4): 391−403. DOI: 10.1016/0013-7952(90)90023-T.

[12] LI Guo-qing, YAN De-tian, ZHUANG Xin-guo, ZHANG Zheng, FU Hai-jiao. Implications of the pore pressure and in situ stress for the coalbed methane exploration in the southern Junggar Basin, China [J]. Engineering Geology, 2019, 262: 105305. DOI: 10.1016/j.enggeo.2019.105305.

[13] ZHENG Lian-ge, RUTQVIST J, BIRKHOLZER J T, LIU Hui-hai. On the impact of temperatures up to 200 °C in clay repositories with bentonite engineer barrier systems: A study with coupled thermal, hydrological, chemical, and mechanical modeling [J]. Engineering Geology, 2015, 197: 278−295. DOI: 10.1016/j.enggeo.2015.08.026.

[14] DAS B, CHATTERJEE R. Wellbore stability analysis and prediction of minimum mud weight for few wells in Krishna-Godavari Basin, India [J]. International Journal of Rock Mechanics and Mining Sciences, 2017, 93: 30 − 37. DOI:

10.1016/j.ijrmms.2016.12.018.

[15] CHEN Shi-da, TANG Da-zhen, TAO Shu, XU Hao, ZHAO Jun-long, FU Hai-jiao, REN Peng-fei. In-situ stress, stress-dependent permeability, pore pressure and gas-bearing system in multiple coal seams in the Panguan area, western Guizhou, China [J]. Journal of Natural Gas Science and Engineering, 2018, 49: 110 − 122. DOI: 10.1016/j.jngse.2017.10.009.

[16] ZHAO Jun, FENG Xia-ting, ZHANG Xi-wei, ZHANG Yan, ZHOU Yang-yi, YANG Cheng-xiang. Brittle-ductile transition and failure mechanism of Jinping marble under true triaxial compression [J]. Engineering Geology, 2018, 232: 160−170. DOI: 10.1016/j.enggeo.2017.11.008.

[17] TANG Yang, OKUBO S, XU Jiang, PENG Shou-jian. Progressive failure behaviors and crack evolution of rocks under triaxial compression by 3D digital image correlation [J]. Engineering Geology, 2019, 249: 172 − 185. DOI: 10.1016/j.enggeo.2018.12.026.

[18] ASADIZADEH M, HOSSAINI M F, MOOSAVI M, MASOUMI H, RANJITH P G. Mechanical characterisation of jointed rock-like material with non-persistent rough joints subjected to uniaxial compression [J]. Engineering Geology, 2019, 260: 105224. DOI: 10.1016/j.enggeo.2019.105224.

[19] MA Lin-jian, LIU Xin-yu, WANG Ming-yang, XU Hong-fa, HUA Rui-ping, FAN Peng-xian, JIANG Shen-rong, WANG Guo-an, YI Qi-kang. Experimental investigation of the mechanical properties of rock salt under triaxial cyclic loading [J]. International Journal of Rock Mechanics and Mining Sciences, 2013, 62: 34 − 41. DOI: 10.1016/j.ijrmms.2013.04.003.

[20] PELLET F L, KESHAVARZ M, AMINI-HOSSEINI K. Mechanical damage of a crystalline rock having experienced ultra high deviatoric stress up to 1.7 GPa [J]. International Journal of Rock Mechanics and Mining Sciences, 2011, 48(8): 1364−1368. DOI: 10.1016/j.ijrmms.2011.09.006.

[21] ZHANG Jun-wen, SONG Zhi-xiang, WANG Shan-yong. Experimental investigation on permeability and energy evolution characteristics of deep sandstone along a three-stage loading path [J]. Bulletin of Engineering Geology and the Environment, 2021, 80(2): 1571 − 1584. DOI: 10.1007/s10064-020-01978-6.

[22] HALLBAUER D K, WAGNER H, COOK N G W. Some observations concerning the microscopic and mechanical behaviour of quartzite specimens in stiff, triaxial compression tests [J]. International Journal of Rock Mechanics and Mining Sciences & Geomechanics Abstracts, 1973, 10(6): 713−726. DOI: 10.1016/0148-9062(73)90015-6.

[23] MEDHURST T P, BROWN E T. A study of the mechanical behaviour of coal for pillar design [J]. International Journal of Rock Mechanics and Mining Sciences, 1998, 35(8): 1087−1105. DOI: 10.1016/S0148-9062(98)00168-5.

[24] WANG Shu-gang, ELSWORTH D, LIU Ji-shan. Mechanical behavior of methane infiltrated coal: The roles of gas desorption, stress level and loading rate [J]. Rock Mechanics and Rock Engineering, 2013, 46(5): 945−958. DOI: 10.1007/s00603-012-0324-0.

[25] GHOLAMI R, RASOULI V. Mechanical and elastic properties of transversely isotropic slate [J]. Rock Mechanics and Rock Engineering, 2014, 47(5): 1763 − 1773. DOI: 10.1007/s00603-013-0488-2.

[26] MASRI M, SIBAI M, SHAO J F, MAINGUY M. Experimental investigation of the effect of temperature on the mechanical behavior of Tournemire shale [J]. International Journal of Rock Mechanics and Mining Sciences, 2014, 70: 185 − 191. DOI: 10.1016/j.ijrmms.2014.05.007.

[27] GAO Quan, TAO Jun-liang, HU Jian-ying, YU Xiong. Laboratory study on the mechanical behaviors of an anisotropic shale rock [J]. Journal of Rock Mechanics and Geotechnical Engineering, 2015, 7(2): 213 − 219. DOI: 10.1016/j.jrmge.2015.03.003.

[28] GHOBADI M H, BABAZADEH R. Experimental studies on the effects of cyclic freezing-thawing, salt crystallization, and thermal shock on the physical and mechanical characteristics of selected sandstones [J]. Rock Mechanics and Rock Engineering, 2015, 48(3): 1001 − 1016. DOI: 10.1007/s00603-014-0609-6.

[29] JIN Chang-yu, YANG Cheng-xiang, FANG Dan, XU Shuai. Study on the failure mechanism of basalts with columnar joints in the unloading process on the basis of an experimental cavity [J]. Rock Mechanics and Rock Engineering, 2015, 48(3): 1275−1288. DOI: 10.1007/s00603-014-0625-6.

[30] ZHOU Xue-jun, BURBEY T J, WESTMAN E. The effect of caprock permeability on shear stress path at the aquifer-caprock interface during fluid injection [J]. International Journal of Rock Mechanics and Mining Sciences, 2015, 77: 1−10. DOI: 10.1016/j.ijrmms.2015.03.023.

[31] MENG Qing-bin, ZHANG Ming-wei, HAN Li-jun, PU Hai, LI Hao. Effects of size and strain rate on the mechanical behaviors of rock specimens under uniaxial compression [J]. Arabian Journal of Geosciences, 2016, 9(8): 1 − 14. DOI: 10.1007/s12517-016-2559-7.

[32] ZOU Chun-jiang, WONG L N Y, LOO J J, GAN B S. Different mechanical and cracking behaviors of single-flawed brittle gypsum specimens under dynamic and quasi-static loadings [J]. Engineering Geology, 2016, 201: 71 − 84. DOI: 10.1016/j.enggeo.2015.12.014.

[33] MA Yi-fei, HUANG Hai-ying. DEM analysis of failure mechanisms in the intact Brazilian test [J]. International Journal of Rock Mechanics and Mining Sciences, 2018, 102: 109−119. DOI: 10.1016/j.ijrmms.2017.11.010.

[34] WANG Z L, SHI H, WANG J G. Mechanical behavior and damage constitutive model of granite under coupling of temperature and dynamic loading [J]. Rock Mechanics and Rock Engineering, 2018, 51(10): 3045−3059. DOI: 10.1007/s00603-018-1523-0.

[35] JIANG T, SHAO J F, XU W Y, ZHOU C B. Experimental investigation and micromechanical analysis of damage and permeability variation in brittle rocks [J]. International Journal of Rock Mechanics and Mining Sciences, 2010, 47(5): 703−713. DOI: 10.1016/j.ijrmms.2010.05.003.

[36] WANG H L, XU W Y, JIA C J, CAI M, MENG Q X. Experimental research on permeability evolution with microcrack development in sandstone under different fluid pressures [J]. Journal of Geotechnical and Geoenvironmental Engineering, 2016, 142(6): 04016014. DOI: 10.1061/(asce)gt.1943-5606.0001462.

[37] HU D W, ZHOU H, ZHANG F, SHAO J F. Evolution of poroelastic properties and permeability in damaged

sandstone [J]. International Journal of Rock Mechanics and Mining Sciences, 2010, 47(6): 962 − 973. DOI: 10.1016/j.ijrmms. 2010.06.007.

[38] XU Peng, YANG Sheng-qi. Permeability evolution of sandstone under short-term and long-term triaxial compression [J]. International Journal of Rock Mechanics and Mining Sciences, 2016, 85: 152 − 164. DOI: 10.1016/j.ijrmms.2016.03.016.

[39] HOU Bing, DIAO Ce, LI Dan-dan. An experimental investigation of geomechanical properties of deep tight gas reservoirs [J]. Journal of Natural Gas Science and Engineering, 2017, 47: 22 − 33. DOI: 10.1016/j.jngse.2017.09.004.

[40] BROWN E T, HOEK E. Trends in relationships between measured in situ stresses and depth [J]. International Journal of Rock Mechanics and Mining Sciences & Geomechanics Abstracts, 1978, 15(4): 211 − 215. DOI: 10.1016/0148-9062(78)91227-5.

[41] FENG Yu, HARRISON J P, BOZORGZADEH N. Uncertainty in in situ stress estimations: A statistical simulation to study the effect of numbers of stress measurements [J]. Rock Mechanics and Rock Engineering, 2019, 52(12): 5071 − 5084. DOI: 10.1007/s00603-019-01891-9.

[42] WANG Q Z, JIA X M, KOU S Q, ZHANG Z X, LINDQVIST P A. The flattened Brazilian disc specimen used for testing elastic modulus, tensile strength and fracture toughness of brittle rocks: Analytical and numerical results [J]. International Journal of Rock Mechanics and Mining Sciences, 2004, 41(2): 245 − 253. DOI: 10.1016/S1365-1609(03)00093-5.

[43] CASTRO J, CICERO S, SAGASETA C. A criterion for brittle failure of rocks using the theory of critical distances [J]. Rock Mechanics and Rock Engineering, 2016, 49(1): 63−77. DOI: 10.1007/s00603-015-0728-8.

[44] HAN Li-jun, HE Yong-nian, ZHANG Hou-quan. Study of rock splitting failure based on Griffith strength theory [J]. International Journal of Rock Mechanics and Mining Sciences, 2016, 83: 116 − 121. DOI: 10.1016/j.ijrmms.2015.12.011.

[45] HSIEH A, DIGHT P, DYSKIN A V. The rock stress memory unrecoverable by the Kaiser effect method [J]. International Journal of Rock Mechanics and Mining Sciences, 2015, 75: 190−195. DOI: 10.1016/j.ijrmms.2015.01.006.

[46] XU Xiang-tao, HUANG Run-qiu, LI Hua, HUANG Qiu-xiang. Determination of poisson's ratio of rock material by changing axial stress and unloading lateral stress test [J]. Rock Mechanics and Rock Engineering, 2015, 48(2): 853 − 857. DOI: 10.1007/s00603-014-0586-9.

[47] UNANDER T E, PAPAMICHOS E, TRONVOLL J, SKJ RSTEIN A. Flow geometry effects on sand production from an oil producing perforation cavity [J]. International Journal of Rock Mechanics and Mining Sciences, 1997, 34(3, 4): 293. e1 − 293. e15. DOI: 10.1016/S1365-1609(97)00217-7.

[48] PARK C, SYNN J H, SHIN H S, CHEON D S, LIM H D, JEON S W. Experimental study on the thermal characteristics of rock at low temperatures [J]. International Journal of Rock Mechanics and Mining Sciences, 2004, 41: 81 − 86. DOI: 10.1016/j.ijrmms.2004.03.023.

[49] GOWD T N, RUMMEL F. Effect of confining pressure on the fracture behaviour of a porous rock [J]. International Journal of Rock Mechanics and Mining Sciences & Geomechanics Abstracts, 1980, 17(4): 225 − 229. DOI: 10.1016/0148-9062(80)91089-X.

[50] ALAM A K M B, NIIOKA M, FUJII Y, FUKUDA D, KODAMA J I. Effects of confining pressure on the permeability of three rock types under compression [J]. International Journal of Rock Mechanics and Mining Sciences, 2014, 65: 49−61. DOI: 10.1016/j.ijrmms.2013.11.006.

[51] SUKPLUM W, WANNAKAO L. Influence of confining pressure on the mechanical behavior of Phu Kradung sandstone [J]. International Journal of Rock Mechanics and Mining Sciences, 2016, 86: 48 − 54. DOI: 10.1016/j.ijrmms.2016.04.001.

[52] JIANG Shui-hua, LI Dian-qing, ZHANG Li-min, ZHOU Chuang-bing. Time-dependent system reliability of anchored rock slopes considering rock bolt corrosion effect [J]. Engineering Geology, 2014, 175: 1 − 8. DOI: 10.1016/j.enggeo.2014.03.011.

[53] XUE Yu-ting, MISHRA B, GAO Dan-qing. Using the relaxation test to study variation in the time-dependent property of rock and the consequent effect on time-dependent roof failure [J]. Rock Mechanics and Rock Engineering, 2017, 50(9): 2521−2533. DOI: 10.1007/s00603-017-1232-0.

[54] LIU Yan-zhu. Pressure rod instability and Lyapunov stability [J]. Mechanics in Engineering, 2002, 24(4): 56 − 59. (in Chinese)

[55] XUE Yun, CHEN Li-qun. Discuss the pressure rod instability and the stability of Lyapunov again [J]. Mechanics in Engineering, 2004, 26(5): 71−72. (in Chinese)

[56] MENG Zhao-ping, LI Guo-qing. Experimental research on the permeability of high-rank coal under a varying stress and its influencing factors [J]. Engineering Geology, 2013, 162: 108−117. DOI: 10.1016/j.enggeo.2013.04.013.

[57] DIEDERICHS M S. The 2003 Canadian Geotechnical Colloquium: Mechanistic interpretation and practical application of damage and spalling prediction criteria for deep tunnelling [J]. Canadian Geotechnical Journal, 2007, 44(9): 1082−1116. DOI: 10.1139/t07-033.

[58] MARTIN C D, CHRISTIANSSON R. Estimating the potential for spalling around a deep nuclear waste repository in crystalline rock [J]. International Journal of Rock Mechanics and Mining Sciences, 2009, 46(2): 219 − 228. DOI: 10.1016/j.ijrmms.2008.03.001.

[59] RANJITH P G, JASINGE D, CHOI S K, MEHIC M, SHANNON B. The effect of CO_2 saturation on mechanical properties of Australian black coal using acoustic emission [J]. Fuel, 2010, 89(8): 2110 − 2117. DOI: 10.1016/j.fuel.2010.03. 025.

[60] NICKSIAR M, MARTIN C D. Evaluation of methods for determining crack initiation in compression tests on low-porosity rocks [J]. Rock Mechanics and Rock Engineering, 2012, 45(4): 607−617. DOI: 10.1007/s00603-012-0221-6.

[61] CHEN Yu-long, ZUO Jian-ping, LIU De-jun, WANG Zhen-bo. Deformation failure characteristics of coal-rock combined body under uniaxial compression: Experimental and numerical investigations [J]. Bulletin of Engineering

Geology and the Environment, 2019, 78(5): 3449 − 3464. DOI: 10.1007/s10064-018-1336-0.

[62] CHEN Yu-long, TENG Jun-yang, SADIQ R A B, ZHANG Ke. Experimental study of bolt-anchoring mechanism for bedded rock mass [J]. International Journal of Geomechanics, 2020, 20(4): 04020019. DOI: 10.1061/(asce)gm.1943-5622.000 1561.

[63] CHEN Yu-long, ZHANG Yu-ning, LI Xue-long. Experimental study on influence of bedding angle on gas permeability in coal [J]. Journal of Petroleum Science and Engineering, 2019, 179: 173 − 179. DOI: 10.1016/j.petrol.2019.04.010.

(Edited by ZHENG Yu-tong)

中文导读

高应力-渗流耦合下深部砂岩的力学行为

摘要：砂岩的力学行为演化特征对岩石工程的应用与实践很重要。为此，本文提出了一种新的深部岩石力学测试方法与概念，以便揭示超千米深井巷道在开挖后围岩力学行为的演化机制。采用GCTS多场耦合伺服系统，对深部砂岩进行了不同围压条件下的高应力-渗流耦合试验，获得的应力-应变及渗透率演化曲线，较好地表征了深部砂岩“三阶段”加载下的力学行为特征。本文发现了“平台”及二次压密现象，并且随着围压的增加，平台的长度逐渐变短，甚至消失。在I阶段，深部砂岩具有显著的刚化效应。在II阶段，深部砂岩的径向变形占据主导地位。此外，定义了瞬态应变围压柔量，该参量曲线呈现出显著的三阶段演化特征。在III阶段，深部砂岩的峰前径向变形超前于轴向变形，峰后则与之相反。另外，发现了径向应变更能灵敏表征渗透率动态变化，并揭示了渗透率曲与应力-应变曲线各阶段之间的对应关系。

关键词：深部效应；应力-应变；“平台”；围压效应；应力-渗流；渗透率